


 Cite this: *RSC Adv.*, 2021, **11**, 6146

PbO₂ modified with TiO₂-NTs composite materials with enhanced OER electrocatalytic activity for Zn electrowinning

 Chen Chen, ^a Xuanbing Wang, ^a Ruidong Xu, ^{*ab} Ying Zhang, ^a Suyang Feng, ^b Ao Ju ^a and Wenhao Jiang ^a

The high oxygen evolution overpotential of the Pb–Ag anode is one of the main reasons for the high energy consumption in Zn electrowinning. PbO₂, owing to its high conductivity, good corrosion resistance and low cost, is widely used as an excellent coating material. In present research, a novel composite Ti/TiO₂-NTs/PbO₂ material was synthesized through a facile anodization, annealing, electrochemical reduction and galvanostatic deposition. The surface morphology, internal structure and the mechanisms of TiO₂-NTs enhancing electrochemical performance were discussed. The results show that the self-organized high aspect ratio TiO₂-NTs with diameter of ~120 nm and length of ~8 μ m were obtained on Ti substrate. The Ti/TiO₂-NTs/PbO₂ composite material exhibits excellent oxygen evolution performance and good stability in Zn electrowinning simulation solution (50 g L⁻¹ Zn²⁺, 150 g L⁻¹ H₂SO₄) at 35 °C. Its oxygen evolution overpotential is only 630 mV under current density 50 mA cm⁻², which is 332 mV lower than that of Pb-0.76 wt% Ag (η = 962 mV) and only increases 22 mV after 5000 cycles of CV scanning. Its outstanding electrochemical performance is mainly ascribed to the introduction of TiO₂-NTs in Pb(CH₃COO)₂ media since it refines the crystal grains, increases the electrochemical surface area, greatly reduces the charge transfer resistance (25.4 Ω cm² to 2.337 Ω cm²) and enhances corrosion resistance. Therefore, the Ti/TiO₂-NTs/PbO₂ material prepared in Pb(CH₃COO)₂ medium may be an ideal anode for Zn electrowinning.

Received 4th October 2020

Accepted 27th January 2021

DOI: 10.1039/d0ra08448d

rsc.li/rsc-advances

1 Introduction

Zinc extraction processes can be classified into hydrometallurgy and pyrometallurgy, and 80% of the world's zinc is extracted by hydrometallurgy.^{1–4} The energy consumption of Zn electrowinning is a key point accounting for the majority of the total energy consumption in the whole process.⁵ Oxygen Evolution Reaction (OER) occurs at the anode in zinc electrowinning, one of effective ways to decrease energy consumption is reducing the oxygen evolution overpotential of the anode material.⁶ It is worth noting that present Pb–Ag alloy anode exhibits many drawbacks including high OER overpotential, low mechanical strength, low service life and consumption of noble element Ag, which limits the advancement of zinc hydrometallurgy.^{7–10} Therefore, it is urgent to design and synthesise a novel energy-saving anode in zinc hydrometallurgy.

Titanium-based coating insoluble anode possesses stable dimensions, high corrosion resistance and long service life,

which have attracted attention from research¹¹ and it has been widely used in hydrometallurgy, electrolytic wastewater, chlor-alkali industry and other fields.^{12–15} PbO₂ is one of the best options for active coatings due to its low price, high conductivity and excellent corrosion resistance in acid solution.^{16–18} However, its shortcoming, such as poor adhesion, large interface resistance and low electrocatalytic activity cannot be ignored.^{19,20} To our best knowledge, Sn, Sb oxide, α -PbO₂ and other conductive layers can usually serve as intermediate layers to prolong service life and enhance OER performance.^{13,20,21} Besides, the active PbO₂ coating doped with foreign elements or active particles, such as Bi,²² Ag,¹¹ RE,¹⁸ SiO₂,²³ ZrO₂,²⁴ Co₃O₄,¹⁴ MnO₂,²⁵ and carbon nanotubes(CNTs)²² can increase its electrocatalytic activity and corrosion resistance.

The discovery of CNTs by Iijima was inspiring the research of other nanomaterials.²⁶ In 1990s, Zwilling and colleagues first reported that titanium could form self-organized nanotubes in electrolytes containing hydrofluoric acid.²⁷ Over the past 20 years, TiO₂ nanotubes (TiO₂-NTs) has been extensively studied, from initial preparation in aqueous solutions to ionic and organic solutions to multiple anodization processes. Up to now, TiO₂-NTs with high aspect ratio and perfect arrangement can be obtained with controllable diameter and length.^{28–32} It possesses larger specific surface area, higher electron mobility, stronger

^aFaculty of Metallurgical and Energy Engineering, Kunming University of Science and Technology, Kunming 650093, China. E-mail: rdxupaper@aliyun.com; Fax: +86 871 65161278; Tel: +86 871 65160072

^bState Key Laboratory of Complex Nonferrous Metal Resources Clean Utilization, Kunming University of Science and Technology, Kunming 650093, China



hydrophilicity and stronger adsorption capacity and higher photoelectric catalytic activity than TiO_2 (quantum size effects), which is widely used in solar cells, electrochromic, sensors, photocatalytic decomposition of water, self-cleaning function and electrolytic wastewater and other fields.³³ It is a n-type semiconductor with wide band gap ($E_g \approx 3.0$ eV) which is appropriate for photocatalytic reactions. However, a large amount of energy is required in the process of the transition of valence electrons to the conduction band becoming free electrons because of the wide band gap, which limit its widely application in the field of electrode materials.³⁴ In recent years, some researches on the conductivity of TiO_2 -NTs have been reported in many literatures, such as crystal directional growth,³⁵ electrodeposition Cu,³⁶ foreign element doping³⁷ and self-doping reduction.³⁸ These methods can increase the carrier concentration of the nanotubes so as to enhance its conductivity, making TiO_2 -NTs possible to be used in an anode materials for zinc electrowinning.

Lead nitrate medium is one of the most fashion media used for PbO_2 electrodeposition. Besides that, lead acetate,³⁹ lead methyl sulfonate,⁴⁰ lead sulfamate,⁴¹ lead fluoroborate⁴² and other media have also been reported. In present research, TiO_2 -NTs may be used in Zn electrowinning anode for the first time. Titanium was selected as the substrate to fabricate TiO_2 -NTs *in situ* as the intermediate layer *via* anodization. Additional anodization, annealing and electrochemical reduction methods were used to enhance the conductivity of the nanotubes and adhesion. PbO_2 was deposited on Ti/TiO_2 -NTs through galvanostatic deposition in lead acetate ($\text{Pb}(\text{CH}_3\text{COO})_2$) medium and lead nitrate ($\text{Pb}(\text{NO}_3)_2$) medium. A novel Ti/TiO_2 -NTs/ PbO_2 material with excellent OER performance and good corrosion resistance was successfully prepared in the $\text{Pb}(\text{CH}_3\text{COO})_2$ medium. The physical structure was studied by XRD and FE-SEM, and the electrochemical performance were tested by LSV, CV, EIS and Tafel. And the mechanisms of TiO_2 -NTs

enhancing OER performance and corrosion resistance were explored.

2 Experimental

2.1 Preparation of Ti/TiO_2 -NTs

Titanium sheet (20 mm × 10 mm × 1 mm) was used to fabricate TiO_2 -NTs *via* anodization. First, the titanium sheet was chemically polished in a mixed solution of HF, HNO_3 and deionized water in a ratio of 1 : 1 : 2 for 10 s. Then it was ultrasonic for 5 min in anhydrous ethanol, acetone and deionized water, respectively, following dried in the air for 20 min. After that, each titanium sheet was anodized 2 times, with titanium sheet as the anode and stainless steel as the cathode. Step 1: the anodization occurred in 100 ml ethylene glycol (EG) solution containing 0.3 wt% NH_4F and 2 vol% deionized water, DC supply voltage 60 V, time 1 h. Step 2: it was transferred to 100 ml ethylene glycol solution containing 5 wt% H_3PO_4 and

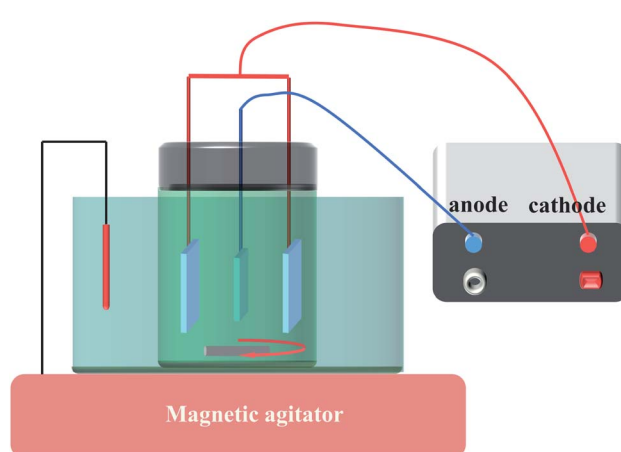


Fig. 2 Experimental installation.

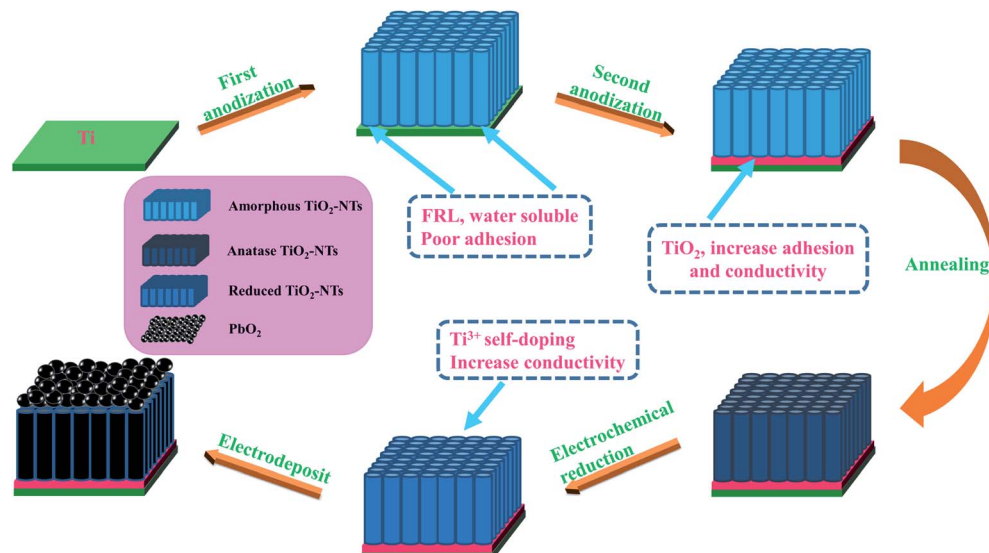


Fig. 1 The general experimental procedures of the work.



oxidized for 1 min so as to eliminate the influence of fluorine-rich layer (FRL) and increase the adhesion of nanotube layer and conductivity.⁴³ Finally, it was annealed for 3 h at an air atmosphere of 450 °C with a heating rate of 3 °C min⁻¹ so that amorphous TiO₂-NTs was converted to anatase.

2.2 Electrodeposition of PbO₂

Before electrodeposition of PbO₂, the electrochemical reduction of TiO₂-NTs was conducted in 0.1 M H₂SO₄ solution for 5 min with the TiO₂-NTs as the cathode and Pt sheet as the anode in order to improve the conductivity of TiO₂-NTs as much as possible, current density 5 mA cm⁻². Then, Ti sheet and Ti/TiO₂-NTs were electrodeposited with PbO₂ in lead acetate medium (I) containing 0.2 M Pb(CH₃COO)₂ and 0.2 M Na(CH₃COO), respectively, and marked as Ti/PbO₂ (I) and Ti/TiO₂-NTs/PbO₂ (I). In addition, PbO₂ was deposited on Ti/TiO₂-NTs in lead nitrate medium (II) containing 0.1 M HNO₃ and 0.2 M Pb(NO₃)₂, and marked as Ti/TiO₂-NTs/PbO₂ (II). Ti sheet and Ti/TiO₂-NTs are the working electrode and stainless steel is the counter electrode, current density 20 mA cm⁻², temperature 40 °C, magnetic stirring speed 300 rpm, and electrodeposition time 1 h. The general experimental procedures are shown in Fig. 1 and the experimental installation are shown in Fig. 2.

2.3 Characterization of materials

The phase structure and surface morphology of the materials were characterized by D/max2200 X-ray diffractometer (XRD, Cu K α radiation) and a Nova Nano-SEM450 field emission scanning electron microscope (FE-SEM) respectively. Linear Sweep Voltammetry (LSV), cyclic voltammetry (CV), electrochemical impedance spectroscopy (EIS) and Tafel plots were tested by electrochemical workstation (CHI760E) under the three electrodes system. The electrolyte is Zn electrowinning simulation solution containing 50 g L⁻¹ Zn²⁺ and 150 g L⁻¹ H₂SO₄ at 35 °C. The composite materials were the working electrodes and only 1 cm² was left as the working area. Mercuric Sulfate

Electrode (MSE) was the reference electrode, and stainless steel was the counter electrode.

2.4 Stability

After Ti/TiO₂-NTs/PbO₂ (I) was prepared, the *i*-*t* curve was tested by chronoamperometry at an anodic potential of 2 V (vs. MSE) and the time of 27 h. Then, its XRD pattern and SEM image were collected in order to deeply analyze the microscopic changes of the material during use. In addition, a 5000-cycle CV scan was adopted, the voltage range was 0–2 V, and the scan rate was 0.05 V s⁻¹, after that, the anodic polarization curve of the material was tested and compared with fresh Ti/TiO₂-NTs/PbO₂ (I).

3 Results and discussion

3.1 The phase structure and surface morphology

The phase composition of the active coating corresponding to Ti/PbO₂ (I), Ti/TiO₂-NTs/PbO₂ (I) and Ti/TiO₂-NTs/PbO₂ (II) materials are shown in Fig. 3. As displayed in the Fig. 3a, The main diffraction peaks of Ti/PbO₂ (I) and Ti/TiO₂-NTs/PbO₂ (I) appear in 36.37°, 58.12°, 60.74° and 77.23° and the corresponding crystal planes are (200), (310), (311) and (400), indicating that the phase only consists of α -PbO₂ (PDF 72-2400), and preferential growth at (200) crystal planes can be seen obviously. The crystal planes (200) and (400) of Ti/TiO₂-NTs/PbO₂ (I) are stronger compared with Ti/PbO₂ (I), suggesting that the introduction of TiO₂-NTs is beneficial to the formation of PbO₂ crystals. When the medium is changed into Pb(NO₃)₂, the phases of Ti/TiO₂-NTs/PbO₂ (II) consist of α -PbO₂ and β -PbO₂ (PDF 41-1492). The α -PbO₂ that appears in 28.57°, 32.62°, 34.31° and 49.64° isn't found in Ti/PbO₂ (I) and Ti/TiO₂-NTs/PbO₂ (I). This may also be because the (200) crystal plane preferentially grows obviously in the Pb(CH₃COO)₂ medium, which leads to the inconspicuous peaks of those angles. Besides that, in Fig. 3b, it can be obtained that the FWHM of Ti/PbO₂ (I) (0.290 rad) is smaller than that of Ti/TiO₂-NTs/PbO₂ (I) (0.320

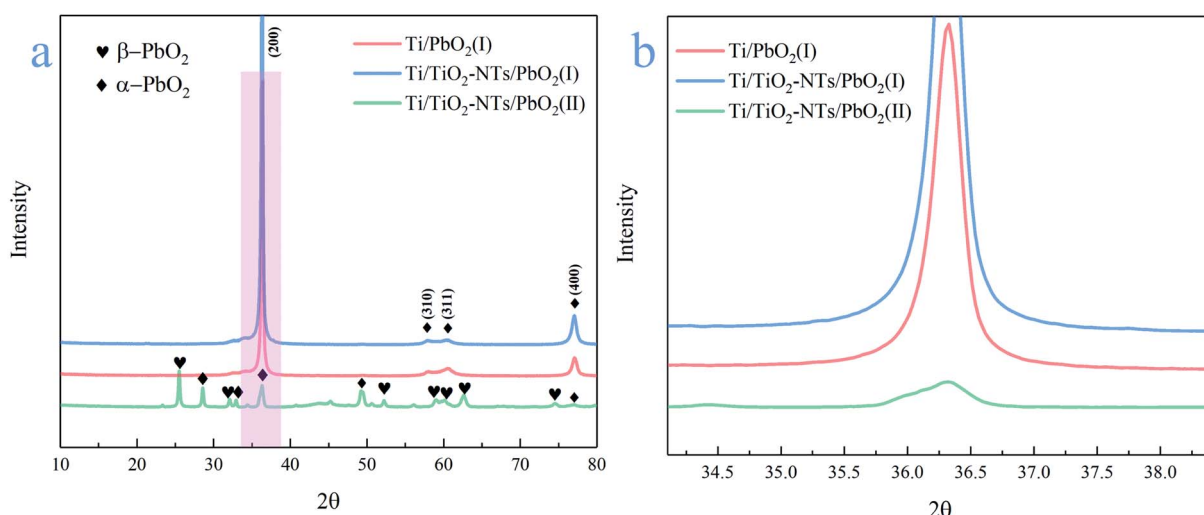


Fig. 3 (a) XRD pattern of different PbO₂ materials; (b) a partial enlarged view of the XRD pattern.



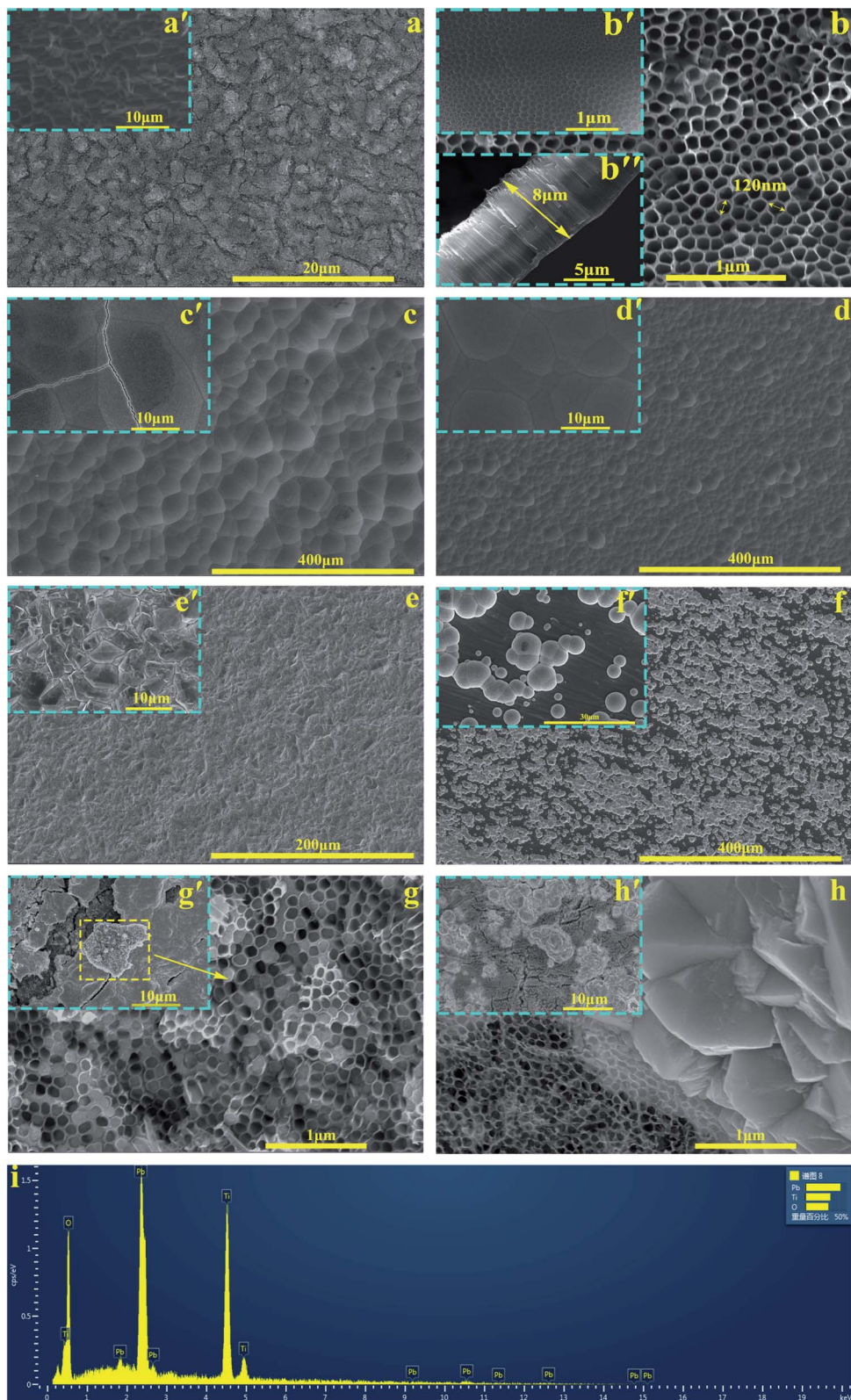


Fig. 4 SEM of different materials: (a) TiO_2 -NTs middle layer at low magnification and (a') Ti sheet after chemical polishing; (b) TiO_2 -NTs at high magnification, (b' and b'') bottom and side of TiO_2 -NTs; (c–e) Ti/PbO_2 (I), Ti/TiO_2 -NTs/ PbO_2 (I) and Ti/TiO_2 -NTs/ PbO_2 (II), deposition time 1 h; (f–h) Ti/PbO_2 (I), Ti/TiO_2 -NTs/ PbO_2 (I) and Ti/TiO_2 -NTs/ PbO_2 (II), deposition time 3 min; (i) EDS of Ti/TiO_2 -NTs/ PbO_2 (I), deposition time 3 min.

rad) in the (200) crystal plane by XRD analysis, revealing that TiO_2 -NTs promotes the formation of smaller PbO_2 grains.

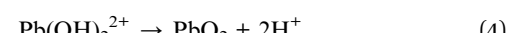
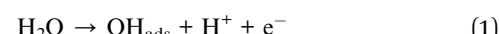
The SEM images of all samples are exhibited in the Fig. 4. The Ti sheet shows a rough surface after chemical polish (Fig. 4a'), which is conducive to the formation of TiO_2 -NTs since the surface electric field on flat surface is so scattered that it is easy to form irregular nanopores.⁴⁴ Fig. 4a presents the surface after anodization, and some obvious change can be seen. Specifically, the detail can be observed in high magnification image (Fig. 4b, b' and b''). A self-organized high aspect ratio TiO_2 -NTs layer is formed onto the surface of Ti sheet with a diameter of ~ 120 nm, length of ~ 8 μm and a closed bottom.

The Fig. 4c and d represent the PbO_2 deposited onto titanium without/with TiO_2 -NTs in the $\text{Pb}(\text{CH}_3\text{COO})_2$ medium respectively. Comparing two images, it can be observed that the introduction of TiO_2 -NTs eliminates the cracks and refines the PbO_2 crystal. In addition, the PbO_2 coating presents a circle shape which is consistent with α - PbO_2 . The result agrees with the XRD pattern. The Fig. 4e is the morphology of PbO_2 deposited onto Ti/TiO_2 -NTs in the $\text{Pb}(\text{NO}_3)_2$ medium. It can be seen that the PbO_2 shows a pyramid shape of β - PbO_2 , which is totally different from that in the $\text{Pb}(\text{CH}_3\text{COO})_2$ medium.

In order to better understand the behaviors of PbO_2 deposition, the SEM images were captured while fixed deposition time was 3 min and shown in Fig. 4f-h. In the Fig. 4f (Ti/PbO_2 , $\text{Pb}(\text{CH}_3\text{COO})_2$), there are only a small amount of PbO_2 on Ti substrate. But it can be seen from Fig. 4g' (Ti/TiO_2 -NTs/ PbO_2 , $\text{Pb}(\text{CH}_3\text{COO})_2$) that the Ti/TiO_2 -NTs surface is covered with a layer of PbO_2 , which demonstrates TiO_2 -NTs promotes the formation of PbO_2 . Moreover, the cross section of the nanotube was collected and shown in Fig. 4g (Ti/TiO_2 -NTs/ PbO_2 , $\text{Pb}(\text{CH}_3\text{COO})_2$). A great amount of nanotube channel is filled with PbO_2 , which has been confirmed in EDS results (Fig. 4i). However, in Fig. 4h (Ti/TiO_2 -NTs/ PbO_2 , $\text{Pb}(\text{NO}_3)_2$) that is the

deposition in the $\text{Pb}(\text{NO}_3)_2$ medium for 3 min, the PbO_2 isn't found at the nanotube orifice, while it exists outside the nanotube. It suggests that PbO_2 may preferentially grow outside the nanotube resulting in a low filling rate of PbO_2 in the nanotube channel. In addition, in the Fig. 4h', PbO_2 does not completely cover Ti/TiO_2 -NTs surface, comparing with Fig. 4g', which means that the deposition rate of PbO_2 in the $\text{Pb}(\text{NO}_3)_2$ medium is slower than in the $\text{Pb}(\text{CH}_3\text{COO})_2$ medium.

In general, the deposition behavior of PbO_2 can be summarized. First of all, TiO_2 -NTs may be able to provide a larger surface area and more nucleation sites, resulting in an increase in nucleation rate and a decrease in PbO_2 grain size. Moreover, it can eliminate the surface crack and increase the adhesion of PbO_2 coating. Secondly, the deposition behavior of PbO_2 in nanotube channel is different in the two media. According to a literature reported by Velichenko,⁴⁵ the electrodeposition mechanism of PbO_2 can be described as following:



According to reactions (1-4), as the electrodeposition of PbO_2 goes on, more H^+ will produce, and the formation of PbO_2 can be inhibited due to decrease of pH. When PbO_2 is electrodeposited onto TiO_2 -NTs, the ion exchange is not timely due to the small diameter of the nanotube. The pH in the nanotube channel will decrease with the development of electrodeposition so that the continuous generation of PbO_2 in the nanotube channel is inhibited. However, in the $\text{Pb}(\text{CH}_3\text{COO})_2$ medium,

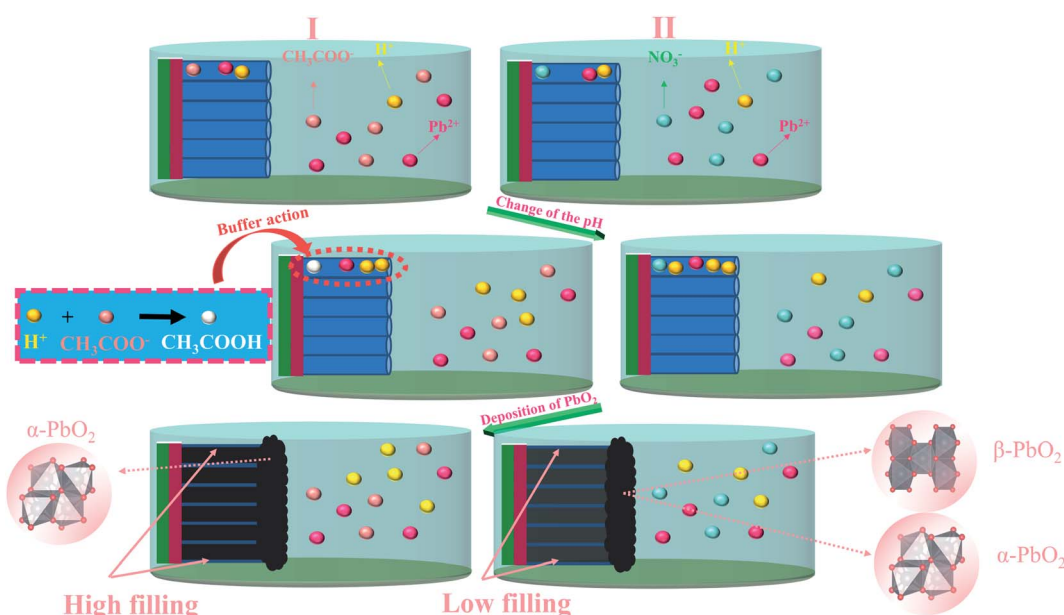


Fig. 5 Schematic diagram of the influence of deposition medium on PbO_2 materials.



the CH_3COO^- can play the role of buffer to effectively hinder the pH reduction. The PbO_2 can be deposited gradually in channel, as shown in the Fig. 5. The nanotube channel has a high filling rate, which can cause the PbO_2 coating and TiO_2 -NTs have a good combination.

3.2 Oxygen evolution activity of the materials

3.2.1 LSV curve analysis. In oxygen evolution kinetics, oxygen evolution overpotential oxygen evolution overpotential is, the easier it is to produce oxygen. In order to study the η parameters of these materials, LSV technology was adopted in simulated Zn electrowinning solution ($50 \text{ g L}^{-1} \text{ Zn}^{2+}$, $150 \text{ g L}^{-1} \text{ H}_2\text{SO}_4$), scanning rate 0.05 V s^{-1} , temperature 35°C . In addition, the LSV curve of Pb-0.76 wt% Ag was also tested in order to compare with it. The measured LSV curves and η value are shown in Fig. 6.

Their OER catalytic activity can be visually compared from Fig. 6a. The catalytic activity from low to high is Ti/TiO_2 -NTs/ PbO_2 (II), Pb-0.76wt%Ag, Ti/PbO_2 (I) and Ti/TiO_2 -NTs/ PbO_2 (I). It can be seen from Fig. 6b that the η of Pb-0.76 wt% Ag is 962 mV. The high η is one of the main reasons for high energy consumption in Zn electrowinning. The η of Ti/PbO_2 (I) is 779 mV, although it is lower than Pb-0.76 wt% Ag, the PbO_2 coating has a lot of cracks and poor adhesion, which is not an ideal electrode. However, Ti/TiO_2 -NTs/ PbO_2 (I) has the best oxygen evolution performance ($\eta = 630 \text{ mV}$). Its η is 149 mV lower than that of Ti/PbO_2 (I) and 332 mV lower than that of Pb-0.76 wt% Ag, indicating that the introduction of TiO_2 -NTs enhances the OER catalytic activity. Moreover, it is worth noting that the η of Ti/TiO_2 -NTs/ PbO_2 (II) ($\eta = 1004 \text{ mV}$) has a significant increase compared with Ti/TiO_2 -NTs/ PbO_2 (I), which shows that $\text{Pb}(\text{CH}_3\text{COO})_2$ medium may be more suitable for electrodeposition of PbO_2 on TiO_2 -NTs in order to improve OER catalytic activity.

3.2.2 CV curves analysis. So far, OER mechanisms have been fully studied through dynamics and density functional theory (DFT), and one of the accepted mechanisms is shown in the Fig. 7.⁴⁶⁻⁴⁹ S represents the active sites on the oxide

electrode, while OH_{ads} and O_{ads} stand for the adsorbable hydroxyl and oxygen-group species, respectively. The S plays a crucial role in the whole reaction path. In the oxide electrode, only active sites can chemically adsorb and desorb intermediate products (OH_{ads} and O_{ads}), thereby providing places for chemical reactions. Therefore, the larger the specific surface area, the more active sites, the stronger the oxygen evolution capacity. The specific surface areas can be qualitatively compared by obtaining the voltammetry charge (q^*) from the integral CV curves, the larger the q^* , the larger the specific surface area, at the same scanning rate (v).²¹

In this work, scan rates 0.01 V s^{-1} , 0.03 V s^{-1} , 0.05 V s^{-1} , 0.07 V s^{-1} and 0.09 V s^{-1} were adopted, and the measured CV curves at 0.05 V s^{-1} are shown in the Fig. 8a. The following relations exist between q^* and v :

$$q^* = q_o^* + kv^{-1/2} \quad (5)$$

$$(q^*)^{-1} = (q_T^*)^{-1} + k' v^{1/2} \quad (6)$$

$$q_T^* = q_o^* + q_i^* \quad (7)$$

The k and k' are constants for the slope, q_T^* is the real charge on the surface of the electrode which consists of the outercharge (q_o^*) and the innercharge (q_i^*). The relationships of q^* versus $v^{-1/2}$ and $(q^*)^{-1}$ versus $v^{1/2}$ is shown in Fig. 8c and d.

In the Fig. 8a, the CV curve of Ti/PbO_2 (I) is smaller than Ti/TiO_2 -NTs/ PbO_2 (I), and Ti/TiO_2 -NTs/ PbO_2 (II) has the smallest CV curve. The calculated q^* at 0.05 V s^{-1} is shown in the Fig. 8b. The q^* of Ti/PbO_2 (I) is 3.586 C cm^{-2} , after the introduction of TiO_2 -NTs, the q^* of Ti/TiO_2 -NTs/ PbO_2 (I) increased to 4.478 C cm^{-2} , which means that TiO_2 -NTs promote the formation of a larger specific surface area PbO_2 coating. This may because TiO_2 -NTs can provide a large surface area for PbO_2 nucleation, and the increase in nucleation rate leads to an increase in electrode surface area. However, the q^* of Ti/TiO_2 -NTs/ PbO_2 (II) is the smallest. The result shows that the specific surface area of PbO_2 electrodeposited in the $\text{Pb}(\text{CH}_3\text{COO})_2$ medium are larger than those in the $\text{Pb}(\text{NO}_3)_2$ medium. It may due to PbO_2 with

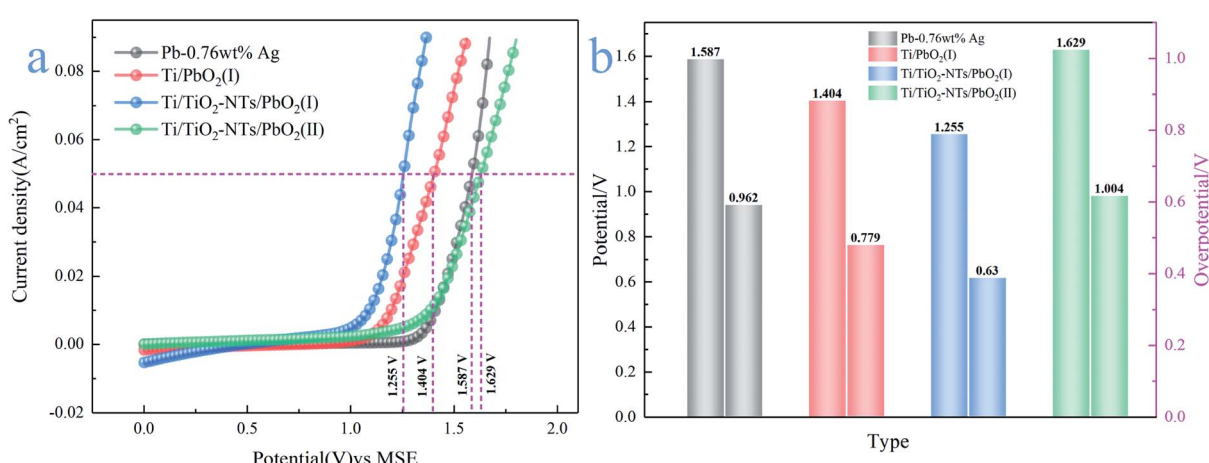


Fig. 6 (a) Anode polarization curve of different PbO_2 materials; (b) oxygen evolution potential and overpotential of different PbO_2 materials.



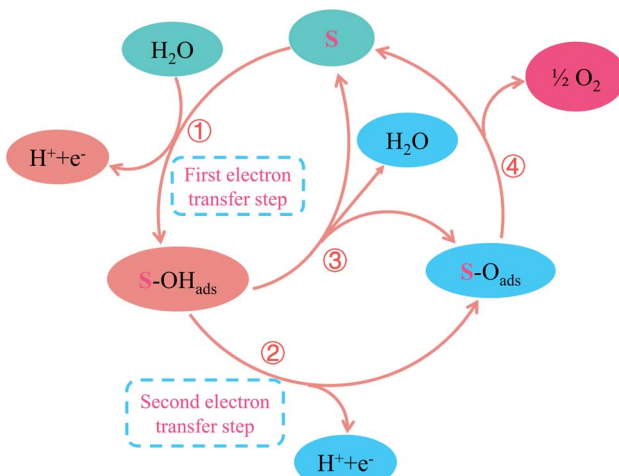


Fig. 7 The oxygen evolution mechanism of PbO_2 materials in acidic solution.

a smaller grain size can be obtained in the $\text{Pb}(\text{CH}_3\text{COO})_2$ medium, resulting in a larger specific surface area. The similar laws about specific surface area at different scan rates also can be found in Fig. 8c and d. These corresponds to LSV curves characteristics in the previous section.

3.2.3 EIS analysis. According to the OER mechanism in the Fig. 7, OER begins with the transfer of the first charge and generates OH_{ads} , then the second charge transfers and generates O_{ads} .⁴⁶ It is worth mentioning that the first charge transfer step is the rate-determining step (RDS) of OER, which has been confirmed by many researchers and is called primary water discharge.⁵⁰ The conductivity of the electrode material determines the rate of charge transfer and affects the rate of OER. Therefore, in order to further study the factors affecting the catalytic activity of OER, EIS technology was adopted at an anodic potential of 1.4 V (vs. MSE). The measured EIS curves are shown in the Fig. 9.

There are two semicircles in the Nyquist plots (Fig. 9a) and two peaks in the Bode plots (Fig. 9b), indicating the existence of two time-constant. The phenomenon exists in the following cases, such as the generation of solid electrolyte interface (SEI)

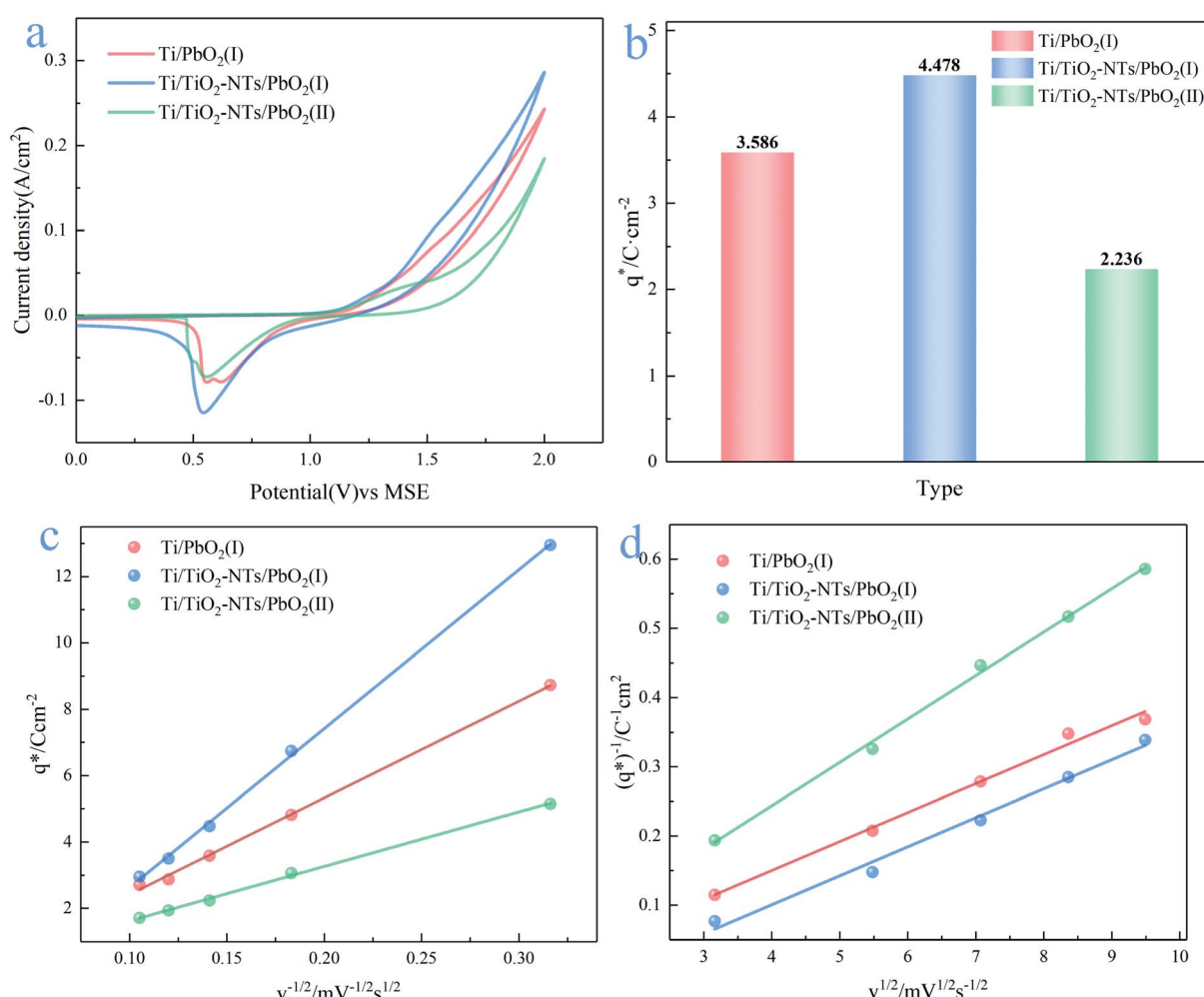


Fig. 8 (a) CV curves of different PbO_2 materials; (b) voltammetry charge of different materials at 0.05 V s^{-1} ; (c) relationship of q^* versus $v^{-1/2}$; (d) relationship of $(q^*)^{-1}$ versus $v^{1/2}$.

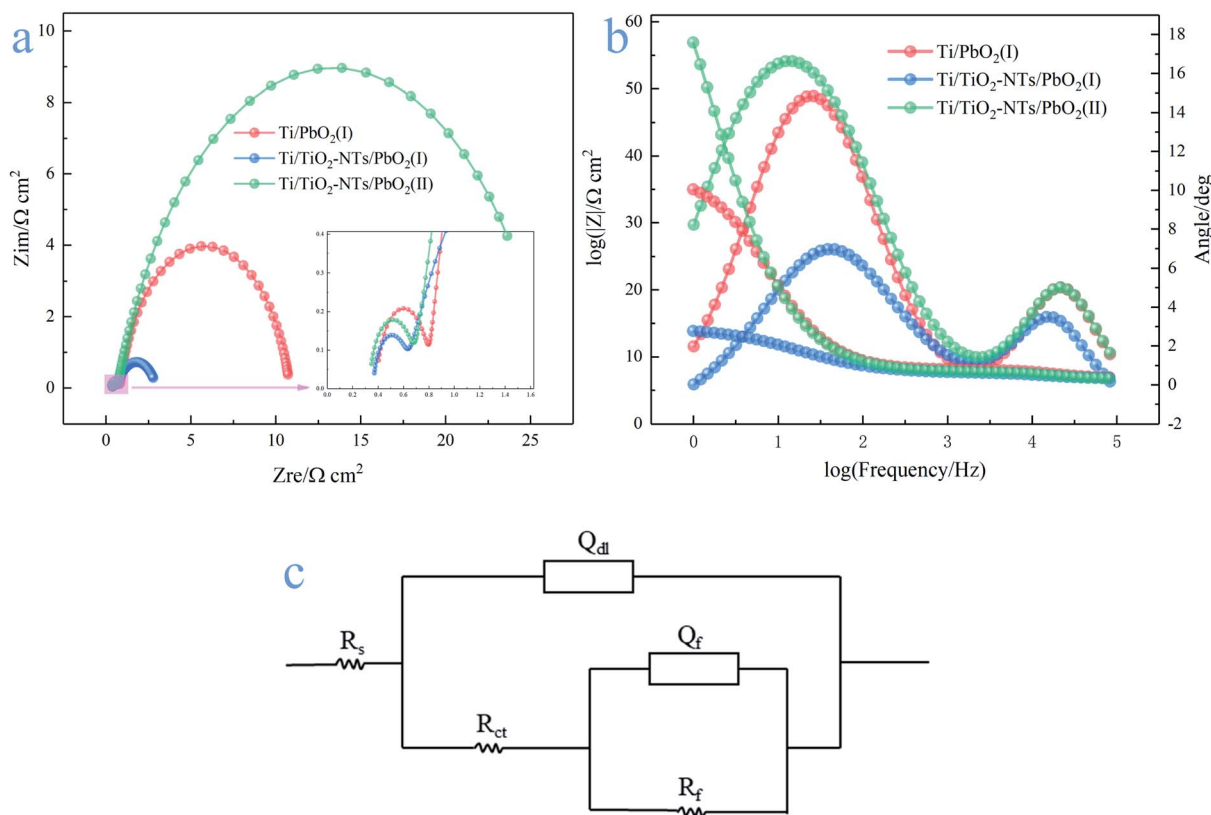


Fig. 9 (a) Nyquist plots of different PbO₂ materials; (b) Bode plots of different PbO₂ materials; (c) equivalent circuit of OER on the PbO₂ materials in the simulated solution (50 g L⁻¹ Zn²⁺, 150 g L⁻¹ H₂SO₄) at 35 °C.

membranes in lithium ion batteries, the occurrence of side reactions in metal corrosion, intermediates adsorption and desorption in the reaction process and so on. Electrochemical impedance spectroscopy usually consists of three parts: the high frequency semicircle is mainly the capacitive behavior due to the above situations, the middle frequency semicircle represents the impedance behavior due to charge transfer, and the straight line at low frequency is the Warburg impedance.⁵¹ The Nyquist plots are calculated using the $R(Q(R(QR)))$ equivalent circuit,⁵² as shown in the Fig. 9c. R_f , R_{ct} and R_s represent adsorption impedance of OH_{ads} and O_{ads}, charge transfer resistance and solution resistance, respectively. Q_f and Q_{dl} are constant phase elements (CPE), because the surface of electrode materials is not an ideal plane, and the electrochemical properties of the electrode surface vary from place to place, resulting in the dispersion of resistance and capacitance. The characteristic values of capacitance can be calculated by the following formulas:⁵³

$$C = Q^{1/n}(R_s^{-1} + R_{ct}^{-1})^{(n-1)/n} \quad (8)$$

When $R_{ct} \gg R_s$

$$C = Q^{1/n}R_s^{(1-n)/n} \quad (9)$$

The simulation results of each parameter in the equivalent circuit are listed in the Table 1. The R_s maintaining around 0.33–0.39 (Ω cm²) indicates the stability of the test solution, and R_f maintains 0.269–0.415 (Ω cm²). Some interesting phenomena are found about R_{ct} . First, by comparing Ti/PbO₂ (I) and Ti/TiO₂-NTs/PbO₂ (I), it can be found that TiO₂-NTs as an intermediate layer reduces R_{ct} (10.01 Ω cm² to 2.337 Ω cm²). This probably due to TiO₂-NTs can provide a large contact area with PbO₂ coating, which reduces the interface resistance, as shown in the Fig. 10. Subsequently, when the electrodeposition medium is changed from Pb(CH₃COO)₂ to Pb(NO₃)₂, the R_{ct} shows a significant increase (2.337 Ω cm² to 25.4 Ω cm²). It may be because the PbO₂ deposited in the Pb(NO₃)₂ medium can't fill

Table 1 Parameter values of different PbO₂ materials obtained by equivalent circuit simulation

Type	$R_s/\Omega\text{ cm}^2$	$R_f/\Omega\text{ cm}^2$	$Q_f/\text{m}\Omega^{-1}\text{ s}^n\text{ cm}^{-2}$	$C_f/\text{mF cm}^{-2}$	$R_{ct}/\Omega\text{ cm}^2$	$Q_{dl}/\text{m}\Omega^{-1}\text{ s}^n\text{ cm}^{-2}$	$C_{dl}/\text{mF cm}^{-2}$
Ti/PbO ₂ (I)	0.389	0.415	0.025 ($n = 1$)	0.025	10.01	4.98 ($n = 0.853$)	5.581
Ti/TiO ₂ -NTs/PbO ₂ (I)	0.363	0.269	0.046 ($n = 1$)	0.046	2.337	18.63 ($n = 0.705$)	41.454
Ti/TiO ₂ -NTs/PbO ₂ (II)	0.334	0.353	0.029 ($n = 1$)	0.029	25.4	7.592 ($n = 0.782$)	9.838

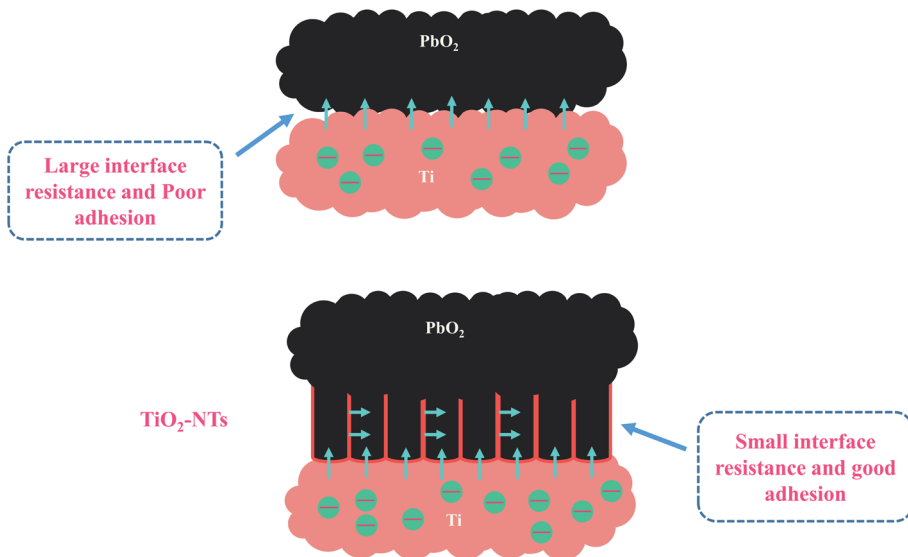


Fig. 10 Schematic diagram of the influence of TiO_2 -NTs on materials.

the nanotube channel well, which isn't conducive to electron transport, as shown in the Fig. 5 in the SEM discussion.

The electrocatalytic activity of $\text{Ti}/\text{TiO}_2\text{-NTs}/\text{PbO}_2$ is compared with some reported materials. As shown in Table 2 and Fig. 11.

It can be seen from Fig. 11 that $\text{Ti}/\text{TiO}_2\text{-NTs}/\text{PbO}_2$ (I) exhibits an excellent OER electrocatalytic activity, and its oxygen evolution overpotential is only 630 mV. This outstanding oxygen evolution performance is mainly attributed to the nanotube structure of TiO_2 -NTs and the choice of lead acetate medium. The nano-channel structure provides a large surface area for PbO_2 electrodeposition, refines the PbO_2 grains, and increases the specific surface area of the deposits. The choice of lead acetate medium can make the nanotube channel better filled, which greatly reduces the internal resistance of the material. Therefore, $\text{Ti}/\text{TiO}_2\text{-NTs}/\text{PbO}_2$ (I) composite material presents an excellent OER electrocatalytic activity.

Table 2 Comparison of related materials for OER electrocatalytic activity

Electrodes	Concentration of H_2SO_4	η (mV (vs. NHE, 50 mA cm^{-2}))	Reference
$\text{Ti}/\text{Sb-SnO}_2/\text{Bi-PbO}_2$	0.5 M	1046	54
$\text{Al}/\text{Pb-PANI-WC}$	1.53 M	941	8
Pure Pb	1.8 M	936	55
$\text{PbO}_2\text{-Co}_3\text{O}_4$	1.63 M	858	56
$\text{PANI/CeO}_2/\text{WC}$	1.53 M	856	57
Pb-CeO_2	1.63 M	826	58
$\text{Pb-Co}_3\text{O}_4$	1.53 M	792	56
3D-Pb-Ag/F-PbO ₂	1.53 M	772	59
Pb-MnO_2	1.63 M	765	60
3D-Ti/PbO ₂	1.53 M	758	14
$\text{PbO}_2\text{-MnO}_2$	1.63 M	719	61
$\text{Ti/PbO}_2\text{-CeO}_2$ -graphite	1.53 M	648	19
$\text{Ti}/\text{TiO}_2\text{-NTs}/\text{PbO}_2$	1.53 M	630	This work

3.3 Corrosion resistance

Long service life of the electrode is necessary, which is one of the effective ways to save cost. Tafel technology can measure the self-corrosion current (i_{corr}) of different PbO_2 electrode materials, which can be used as one of the criteria to evaluate the service life. The lower the self-corrosion current, the better the corrosion resistance of the electrode. The Tafel plots measured in the simulated solution are shown in Fig. 12a, the temperature is 35 °C, and the scanning rate is 0.001 V s⁻¹. The self-corrosion current obtained by electrochemical workstation analysis is shown in Fig. 12b.

It can be seen from the Fig. 12b that the self-corrosion current of Ti/PbO_2 (I), $\text{Ti}/\text{TiO}_2\text{-NTs}/\text{PbO}_2$ (I) and $\text{Ti}/\text{TiO}_2\text{-NTs}/\text{PbO}_2$ (II) are 2.474×10^{-3} , 7.432×10^{-4} and 6.636×10^{-4} (A cm⁻²) respectively. The self-corrosion current of $\text{Ti}/\text{TiO}_2\text{-NTs}/\text{PbO}_2$ (I) is smaller than that of Ti/PbO_2 (I), which indicates that TiO_2 -NTs as an intermediate layer can increase corrosion resistance. It may be because TiO_2 -NTs can effectively prevent the electrolyte from contacting and corroding the Ti substrate, and it can also eliminate the surface cracks of the PbO_2 coating. In addition, the i_{corr} of $\text{Ti}/\text{TiO}_2\text{-NTs}/\text{PbO}_2$ (II) has slight decrease compared with $\text{Ti}/\text{TiO}_2\text{-NTs}/\text{PbO}_2$ (I), which may be associated with the different crystal structure of PbO_2 , but the too high oxygen evolution overpotential indicates that it is not an ideal anode for Zn electrowinning.

3.4 Stability of the $\text{Ti}/\text{TiO}_2\text{-NTs}/\text{PbO}_2$ (I)

In order to test the stability of $\text{Ti}/\text{TiO}_2\text{-NTs}/\text{PbO}_2$ (I), a 27 h chronoamperometry was performed under a 2 V anodic potential, and the XRD pattern and SEM images were collected after the test. In addition, a 5000-cycle CV scan was adopted, the voltage was 0–2 V, and the scan rate was 0.05 V s⁻¹, and then the LSV curve of $\text{Ti}/\text{TiO}_2\text{-NTs}/\text{PbO}_2$ (I) was measured. The results are shown in Fig. 13.



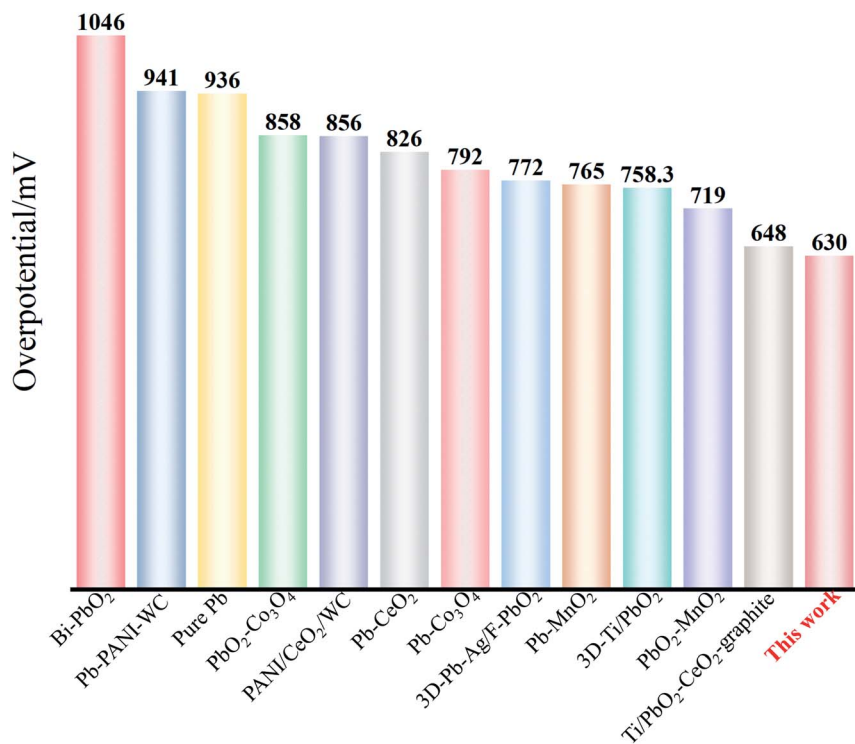


Fig. 11 Oxygen evolution overpotentials of different composite materials at 50 mA cm^{-2} .

It can be seen from Fig. 13a that the current density increases slightly with time. After 27 h, it increases from 271.7 mA cm^{-2} to 291.1 mA cm^{-2} , which indicates that the OER electrocatalytic activity of Ti/TiO₂-NTs/PbO₂ (I) is enhanced. After the 27 h chronoamperometry test, as shown in Fig. 13b, it can be observed that the XRD pattern of Ti/TiO₂-NTs/PbO₂ (I) only appears a new characteristic peak located at 32.62° . This corresponds to the (002) crystal plane of α -PbO₂ (PDF 72-2400), which means that no new substance is generated. Interestingly, the surface becomes rougher and presents a cone shape similar

to β -PbO₂ (Fig. 13c and d), which is beneficial to the increase of the specific surface area to enhance the OER electrocatalytic activity. This conforms to the law presented in Fig. 13a. In addition, in Fig. 13e, Ti/TiO₂-NTs/PbO₂ (I) still exhibits a stable anodic polarization curve after 5000 cycles of CV scanning, and its oxygen evolution overpotential has only increased by 22 mV at 50 mA cm^{-2} compared with fresh Ti/TiO₂-NTs/PbO₂ (I). All these indicate that the composite material possesses an excellent stability and long-term application potential in acidic media.

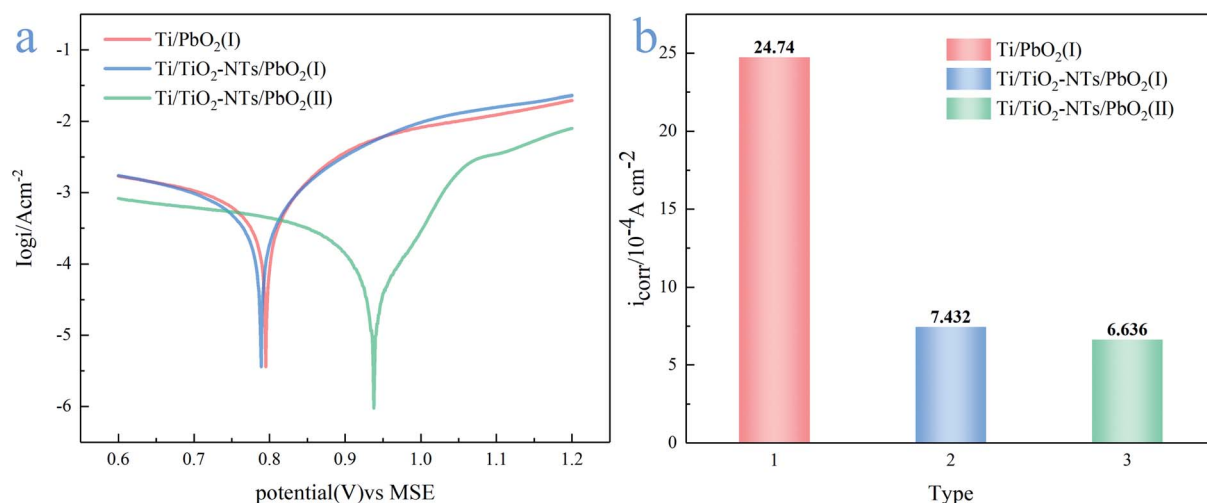


Fig. 12 (a) Tafel plots of different PbO₂ materials at scan rate 0.001 V s^{-1} ; (b) self-corrosion current of different PbO₂ materials in the simulated solution at 35°C .



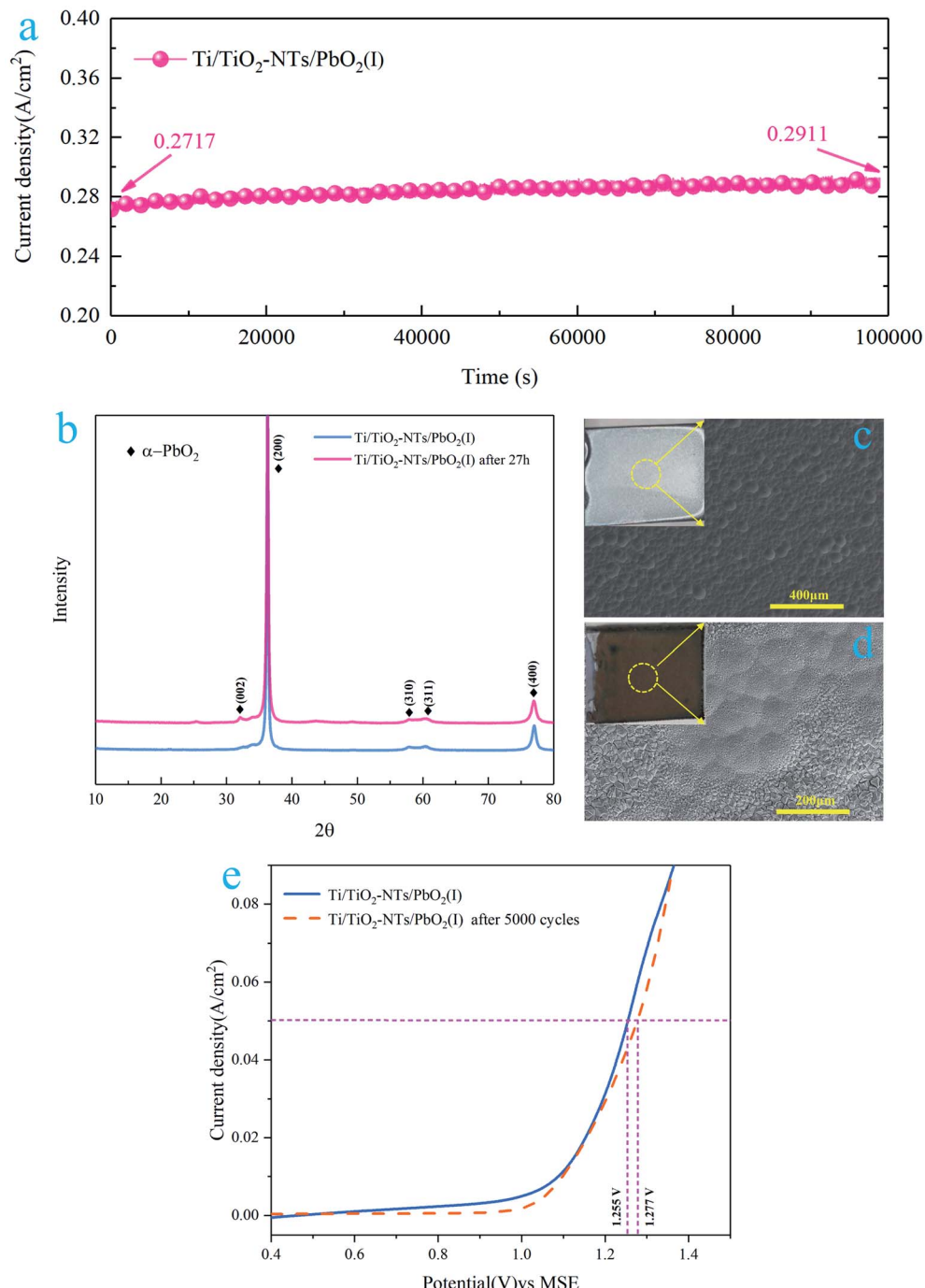


Fig. 13 (a) Chronoamperometry curve of $\text{Ti/TiO}_2\text{-NTs/PbO}_2$ (I); (b) XRD pattern of $\text{Ti/TiO}_2\text{-NTs/PbO}_2$ (I) after 27 h chronoamperometry test; (c) SEM image of fresh $\text{Ti/TiO}_2\text{-NTs/PbO}_2$ (I); (d) SEM image of $\text{Ti/TiO}_2\text{-NTs/PbO}_2$ (I) after 27 h chronoamperometry test; (e) LSV curve of $\text{Ti/TiO}_2\text{-NTs/PbO}_2$ (I) after 5000 cycles of CV scan.

4 Conclusion

On the whole, a novel $\text{Ti/TiO}_2\text{-NTs/PbO}_2$ composite material for Zn electrowinning was successfully synthesized in the $\text{Pb}(\text{CH}_3\text{COO})_2$ medium. $\text{TiO}_2\text{-NTs}$ with a diameter of ~ 120 nm, a length of $\sim 8 \mu\text{m}$ and uniform arrangement was obtained *via* anodization in ethylene glycol electrolyte containing 0.3wt% NH_4F

and 2% vol deionized water. In the $\text{Pb}(\text{CH}_3\text{COO})_2$ medium, $\text{TiO}_2\text{-NTs}$ as an intermediate layer can make the PbO_2 coating have small grains, few cracks, and large surface area (4.478 C cm^{-2} and $41.454 \text{ mF cm}^{-2}$). Moreover, $\text{TiO}_2\text{-NTs}$ channel can be well filled by PbO_2 , which results in a low charge transfer resistance ($2.337 \Omega \text{ cm}^2$). In addition, it can act as a barrier layer to increase the corrosion resistance ($24.74 \times 10^{-4} \text{ A cm}^{-2}$ to $7.432 \times 10^{-4} \text{ A cm}^{-2}$). Therefore, the electrochemical



performance is enhanced through the modification of TiO_2 -NTs. The oxygen evolution overpotential of Ti/TiO_2 -NTs/ PbO_2 (I) ($\eta = 630$ mV) is 332 mV lower than that of Pb-0.76 wt% Ag ($\eta = 962$ mV) under current density 50 mA cm^{-2} in the Zn electrowinning simulation solution ($50 \text{ g L}^{-1} \text{ Zn}^{2+}$, $150 \text{ g L}^{-1} \text{ H}_2\text{SO}_4$) at 35°C and only increases 22 mV after 5000 cycles of CV scanning. These results indicate that Ti/TiO_2 -NTs/ PbO_2 prepared in $\text{Pb}(\text{CH}_3\text{COO})_2$ medium may be an ideal Zn electrowinning anode material.

Conflicts of interest

There are no conflicts to declare.

Acknowledgements

The authors gratefully acknowledge the financial support of the National Natural Science Foundation of China (Project No. 51874154), the Key Project of Yunnan Province Science and Technology Plan of China (Project No. 2014FA024), the Specialized Research Fund for the Doctoral Program of the Ministry of Education of China (Project No. 20125314110011), and the Analysis and Measurement Fund (2019M20182102009) of Kunming University of Science and Technology.

References

- W. Wang, T. Yuan, R. Li, X. Zhu, H. Li, W. Lin, L. Li and D. Zheng, *J. Electroanal. Chem.*, 2019, **847**.
- P. Li, Q. Cai and B. Wei, *Eng. Failure Anal.*, 2006, **13**, 876–885.
- E. Abkhoshk, E. Jorjani, M. S. Al-Harahsheh, F. Rashchi and M. Naazeri, *Hydrometallurgy*, 2014, **149**, 153–167.
- Y. Haitao, C. Buming, L. Jianhua, G. Zhongcheng, Z. Yongchun and X. ruidong, *Rare Met. Mater. Eng.*, 2014, **43**, 2889–2892.
- W. Wang, R. Li, T. Yuan, X. Zhu, H. Li, W. Lin and L. Li, *Hydrometallurgy*, 2020, **192**.
- W. Zhang and G. Houlachi, *Hydrometallurgy*, 2010, **104**, 129–135.
- N. Sorour, C. Su, E. Ghali and G. Houlachi, *Electrochim. Acta*, 2017, **258**, 631–638.
- R. D. Xu, L. P. Huang, J. F. Zhou, P. Zhan, Y. Y. Guan and Y. Kong, *Hydrometallurgy*, 2012, **125–126**, 8–15.
- Y. Li, L. X. Jiang, X. J. Lv, Y. Q. Lai, H. L. Zhang, J. Li and Y. X. Liu, *Hydrometallurgy*, 2011, **109**, 252–257.
- L. Yanqing, J. Liangxing, L. Jie, Z. Shuiping, L. Xiaojun, P. Hongjian and L. Yexiang, *Hydrometallurgy*, 2010, **102**, 81–86.
- S. Chen, B. Chen, S. Wang, W. Yan, Y. He, Z. Guo and R. Xu, *J. Alloys Compd.*, 2020, **815**.
- J. Yang, Q. Wang, J. Zhou, Q. Shen, L. Cao and J. Yang, *Sep. Purif. Technol.*, 2020, **250**.
- Y. Zheng, W. Su, S. Chen, X. Wu and X. Chen, *Chem. Eng. J.*, 2011, **174**, 304–309.
- X. Wang, R. Xu, S. Feng, B. Yu and B. Chen, *RSC Adv.*, 2020, **10**, 1351–1360.
- R. K. Karlsson and A. Cornell, *Chem. Rev.*, 2016, **116**, 2982–3028.
- Y. Yao, G. Teng, Y. Yang, C. Huang, B. Liu and L. Guo, *Sep. Purif. Technol.*, 2019, **211**, 456–466.
- M. Xu, Z. Wang, F. Wang, P. Hong, C. Wang, X. Ouyang, C. Zhu, Y. Wei, Y. Hun and W. Fang, *Electrochim. Acta*, 2016, **201**, 240–250.
- Q. Dai, Y. Xia and J. Chen, *Electrochim. Acta*, 2016, **188**, 871–881.
- C. Zhang, J. Liu and B. Chen, *Ceram. Int.*, 2018, **44**, 19735–19742.
- C. Tang, Y. Lu, F. Wang, H. Niu, L. Yu and J. Xue, *Electrochim. Acta*, 2020, **331**.
- W. Zhao, J. Xing, D. Chen, Z. Bai and Y. Xia, *RSC Adv.*, 2015, **5**, 26530–26539.
- L. Chang, Y. Zhou, X. Duan, W. Liu and D. Xu, *J. Taiwan Inst. Chem. Eng.*, 2014, **45**, 1338–1346.
- J. Bao, N. Lin, J. Guo, W. Gao, Z. Liu and H. Lin, *J. Colloid Interface Sci.*, 2020, **574**, 377–384.
- A. B. Velichenko, V. A. Knysh, T. V. Luk'yanenko, Y. A. Velichenko and D. Devilliers, *Mater. Chem. Phys.*, 2012, **131**, 686–693.
- Y. Li, L. Jiang, F. Liu, J. Li and Y. Liu, *RSC Adv.*, 2014, **4**, 24020–24028.
- S. Iijima, *Nature*, 1991, **354**, 56–58.
- V. Zwilling, E. Darque-Ceretti, A. Boutry-Forveille, D. David, M. Y. Perrin and M. Aucouturier, *Surface and Interface Analysis*, 1999.
- S. P. Albu, A. Ghicov, J. M. Macak and P. Schmuki, *Phys. Status Solidi RRL*, 2007, **1**, R65–R67.
- I. Paramasivam, J. M. Macak, T. Selvam and P. Schmuki, *Electrochim. Acta*, 2008, **54**, 643–648.
- D. Wang, B. Yu, C. Wang, F. Zhou and W. Liu, *Adv. Mater.*, 2009, **21**, 1964–1967.
- R. Beranek, H. Hildebrand and P. Schmuki, *J. Electrochem. Soc.*, 2003, **6**, B12–B14.
- J. M. Macak, S. P. Albu and P. Schmuki, *Phys. Status Solidi RRL*, 2007, **1**, 181–183.
- P. Roy, S. Berger and P. Schmuki, *Angew. Chem., Int. Ed.*, 2011, **50**, 2904–2939.
- X. Chang, S. S. Thind and A. Chen, *ACS Catal.*, 2014, **4**, 2616–2622.
- K. Aijo John, J. Naduvath, S. Mallick, T. Shripathi, M. Thankamoniama and R. R. Philip, *Nanoscale*, 2015, **7**, 20386–20390.
- G. Zhao, Y. Zhang, Y. Lei, B. Lv, J. Gao, Y. Zhang and D. Li, *Environmental Science & Technology*, 2010.
- J. Zhang, Y. Li, Y. Zhang, X. Qian, R. Niu, R. Hu, X. Zhu, X. Wang and J. Zhu, *Nano Energy*, 2018, **43**, 91–102.
- J. M. Macak, B. G. Gong, M. Hueppe and P. Schmuki, *Adv. Mater.*, 2007, **19**, 3027–3031.
- R. Inguanta, F. Vergottini, G. Ferrara, S. Piazza and C. Sunseri, *Electrochim. Acta*, 2010, **55**, 8556–8562.
- I. Sirés, C. T. J. Low, C. Ponce-de-León and F. C. Walsh, *Electrochim. Acta*, 2010, **55**, 2163–2172.
- H. Liu, S. Yu, T. Shen, S. Tong and C. Ma, *Sep. Purif. Technol.*, 2014, **132**, 27–32.



42 X. Zhong, F. Chen, H. Nie, R. Wang and Z. Xu, *Hydrometallurgy*, 2019, **190**.

43 D. Yu, X. Zhu, Z. Xu, X. Zhong, Q. Gui, Y. Song, S. Zhang, X. Chen and D. Li, *ACS Appl. Mater. Interfaces*, 2014, **6**, 8001–8005.

44 G. Z. Shiqi Li, D. Guo, L. Yu and W. Zhang, *J. Phys. Chem. C*, 2009, **113**, 12759–12765.

45 A. B. Velichenko, R. Amadelli, E. V. Gruzdeva, T. V. Luk'yanenko and F. I. Danilov, *J. Power Sources*, 2009, **191**, 103–110.

46 Q. Feng, Q. Wang, Z. Zhang, Y. Xiong, H. Li, Y. Yao, X.-Z. Yuan, M. C. Williams, M. Gu, H. Chen, H. Li and H. Wang, *Appl. Catal., B*, 2019, **244**, 494–501.

47 J. Rossmeisl, A. Logadottir and J. K. Nørskov, *Chem. Phys.*, 2005, **319**, 178–184.

48 S. Laha, Y. Lee, F. Podjaski, D. Weber, V. Duppel, L. M. Schoop, F. Pielnhofer, C. Scheurer, K. Müller, U. Starke, K. Reuter and B. V. Lotsch, *Adv. Energy Mater.*, 2019, **9**, 1803795.

49 H. Over, *Chem. Rev.*, 2012, **112**, 3356–3426.

50 F. R. Costa, D. V. Franco and L. M. Da Silva, *Electrochim. Acta*, 2013, **90**, 332–343.

51 Y. Chen, Y. Zhang, B. Chen, Z. Wang and C. Lu, *J. Power Sources*, 2014, **256**, 20–27.

52 S. Li, F. Wang, M. Xu, Y. Wang, W. Fang and Y. Hu, *J. Electrochem. Soc.*, 2013, **160**, E44–E48.

53 B. Hirschorn, M. E. Orazem, B. Tribollet, V. Vivier, I. Frateur and M. Musiani, *Electrochim. Acta*, 2010, **55**, 6218–6227.

54 W. Yang, W. Yang and X. Lin, *Appl. Surf. Sci.*, 2012, **258**, 5716–5722.

55 Y. S. I. Ivanov and Z. Noncheva, *Hydrometallurgy*, 2000, **57**, 125–139.

56 J. Zhang, R. Xu, B. Yu, Y. He, Y. Li and Z. Qin, *RSC Adv.*, 2017, **7**, 49166–49176.

57 L. Jin, H. Huang, Y. Fei, H. Yang, H. Zhang and Z. Guo, *Hydrometallurgy*, 2018, **176**, 201–207.

58 Z. W. Wenjun Wang and D. Zheng, *Hydrometallurgy*, 2019, **183**, 221–229.

59 B. Chen, W. Yan, Y. He, H. Huang, H. Leng, Z. Guo and J. Liu, *J. Electrochem. Soc.*, 2019, **166**, E119–E128.

60 R. Ma, S. Cheng, X. Zhang, S. Li, Z. Liu and X. Li, *Hydrometallurgy*, 2016, **159**, 6–11.

61 R. X. Jiong Wang, *Materials Reports*, 2017, **8**, 35–40.

